Observation of chiral and slow plasmons in twisted bilayer graphene

https://doi.org/10.1038/s41586-022-04520-8

Received: 15 February 2021

Accepted: 4 February 2022

Tianye Huang[1,8], Xuecou Tu[1,8], Changqing Shen[2], Binjie Zheng[1], Junzhuan Wang[1], Hao Wang[3], Kaveh Khaliji[4], Sang Hyun Park[4], Zhiyong Liu[5], Teng Yang[5], Zhidong Zhang[5], Lei Shao[3], Xuesong Li[2,6]✉, Tony Low[4,7]✉, Yi Shi[1]✉ & Xiaomu Wang[1]✉

Moiré superlattices have led to observations of exotic emergent electronic properties such as superconductivity and strong correlated states in small-rotation-angle twisted bilayer graphene (tBLG)[1,2]. Recently, these findings have inspired the search for new properties in moiré plasmons. Although plasmon propagation in the tBLG basal plane has been studied by near-field nano-imaging techniques[3–7], the general electromagnetic character and properties of these plasmons remain elusive. Here we report the direct observation of two new plasmon modes in macroscopic tBLG with a highly ordered moiré superlattice. Using spiral structured nanoribbons of tBLG, we identify signatures of chiral plasmons that arise owing to the uncompensated Berry flux of the electron gas under optical pumping. The salient features of these chiral plasmons are shown through their dependence on optical pumping intensity and electron fillings, in conjunction with distinct resonance splitting and Faraday rotation coinciding with the spectral window of maximal Berry flux. Moreover, we also identify a slow plasmonic mode around 0.4 electronvolts, which stems from the interband transitions between the nested subbands in lattice-relaxed AB-stacked domains. This mode may open up opportunities for strong light–matter interactions within the highly sought after mid-wave infrared spectral window[8]. Our results unveil the new electromagnetic dynamics of small-angle tBLG and exemplify it as a unique quantum optical platform.

The moiré superlattice in twisted bilayer graphene (tBLG) significantly alters the electronic properties of its constituent structures[9–12], which are predicted to support new emerging collective electromagnetic oscillations[7,13–17]. Under small twist angle, the superlattice is featured with periods of up to tens of nanometres. In contrast to nano-imaging[18,19], an alternative way to investigate the plasmon is by measuring the far-field spectral scattering attributes of plasmonic resonators[20,21]. In these resonators, tBLG is patterned into mesoscopic scale structures, in which the edges of these structures are launching sites for surface plasmons, whose spectral resonances are defined by the sizes of their features. Tuning the geometrical sizes (approximately 80–240 nm) and studying their infrared extinction by Fourier transform infrared (FTIR) spectroscopy enables the systematic characterization of these plasmon modes. This approach provides access to a large infrared spectral window not limited by the availability of laser sources. Probing of the far-field scattering phases can also prove useful for the study of chiral electromagnetic responses in moiré plasmonics. A key challenge to perform such exploration lies in obtaining large-area, high-quality tBLG samples. To date, small-angle tBLG samples have been mainly achieved by a 'tear-and-stack' transfer process, which primarily focuses on optimization of a small-area ordered moiré superlattice for electronic transport investigation.

In our study, we prepared and optimized macroscopic tBLG samples from single-crystalline graphene produced by chemical vapour deposition (CVD). The large sample areas (up to hundreds of micrometres) make possible the fabrication of nanostructured surface plasmon resonators for FTIR spectroscopies. Figure 1a schematically shows the preparation process of small-angle tBLG. The two constituent graphene layers from the same CVD single crystal were successively stacked with a small misorientation angle. Figure 1c shows a typical Raman spectrum of the as-prepared tBLG in Fig. 1b. In addition to the G band near 1,584 cm^{-1}, a R' peak near 1,625 cm^{-1} is observed in the tBLG samples with twist angle from 30 to 0.8° (Extended Data Fig. 1). This new peak was attributed to an intravalley double-resonance scattering process, which was found to be dominant in a moiré superlattice[22]. It probes the sample quality (Methods). Figure 1d, e shows the Raman mapping of the intensity of peaks G and R' in the sample, and the presence of a uniform R' peak implies that the moiré superlattice is long-range ordered in that region. To obtain the highest data quality, we only performed experiments on sample regions with prominent R' Raman signals. In fact, the reported new plasmon modes cannot be observed in samples with non-apparent R' peaks (Extended Data Fig. 2). For studying the plasmons, we further patterned the samples into nanoribbons.

---

[1]School of Electronic Science and Engineering, Nanjing University, Nanjing, China. [2]School of electronic science and engineering, University of Electronic Science and Technology of China, Chengdu, China. [3]Beijing Computational Science Research Centre, Beijing, China. [4]Department of Electrical & Computer Engineering, University of Minnesota, Minneapolis, MN, USA. [5]Shenyang National Laboratory for Materials Science, Institute of Metal Research, Chinese Academy of Sciences, Shenyang, China. [6]Shenzhen Institute for Advanced Study, University of Electronic Science and Technology of China, Shenzhen, China. [7]Department of Physics, University of Minnesota, Minneapolis, MN, USA. [8]These authors contributed equally: Tianye Huang, Xuecou Tu. ✉e-mail: lxs@uestc.edu.cn; tlow@umn.edu; yshi@nju.edu.cn; xiaomu.wang@nju.edu.cn

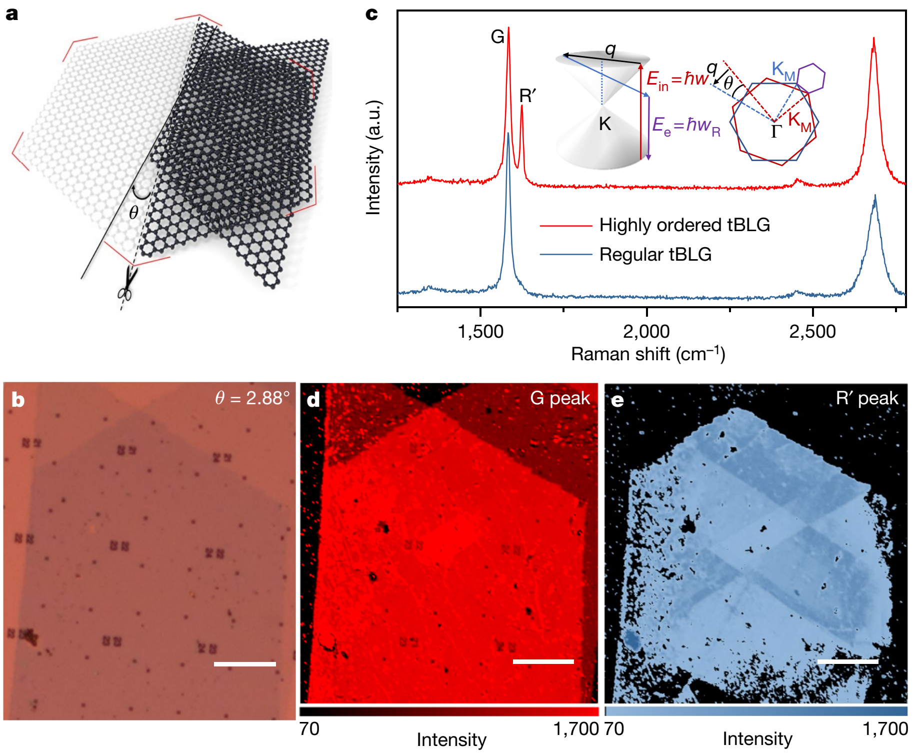

Fig. 1 | Twisted bilayer graphene with highly ordered moiré superlattice. **a**, Schematic of the preparation of small-angle tBLG from a large-area CVD graphene single crystal. **b**, Optical microscope image of a typical tBLG sample with 2.88° twist angle. Scale bar, 100 μm. **c**, Raman spectrum of the sample in **b** when excited by a continuous-wave laser at a wavelength of 514 nm. In addition to the first-order-allowed G band (approximately 1,584 cm^{-1}), an R' peak (centred at around 1,625 cm^{-1}) involving an intravalley double resonance process is observed. The Raman spectrum of a regular tBLG is also shown for comparison. Inset: schematics of the origin of R' peak. Raman emission results from the combination of elastic electron scattering by the moiré potential and inelastic scattering by optical phonons. The BZs of the top and bottom graphene layers rotated away from each other by a small angle θ show the momentum transfer due to moiré superlattice scattering. **d**, **e**, Raman intensity mapping of the G peak (**d**) and R' peak (**e**) of the sample in **b**. The existence of a uniform R' peak reflects the long-range highly ordered moiré superlattice. Scale bars, 100 μm.

We also moderately doped the samples with hydrochloric acid, and a uniform carrier density of around 2×10^{12} cm^{-2} was obtained (Extended Data Fig. 3).

Chiral plasmon mode in tBLG

An object has chirality when its mirror image is not identical to itself. It is achieved when certain symmetries are collectively broken[23]. Our experiments revealed a new chiral plasmon mode (that is, the surface electromagnetic waves show non-reciprocal propagation) within tBLG. This can be traced to the broken inversion symmetry of tBLG as required by the physical chirality due to the twist angle, that is, intuitively, the tBLG twist angle θ is not identical to that of $-\theta$, and its optical signatures are manifested in an observed circular dichroism (CD)[24]. Accompanying the broken inversion symmetry will be a finite Berry curvature, which, in the 'magic angle' (1.08°) limit (the focus of our study), can be most pronounced. To examine the optical properties of tBLG, we first calculated its optical conductivity σ_{xx} (Extended Data Fig. 4). Experimentally, the loss function, defined as the imaginary part of the inverse dielectric function $L=-\mathrm{Im}(1/\varepsilon_{\mathrm{RPA}}(q,\omega))$ (where $\varepsilon_{\mathrm{RPA}}$ is the dielectric constant with momentum q and at frequency ω), is a measure of the plasmon excitations. Figure 2a presents an intensity plot of the loss function of tBLG in the low-energy spectral range. In addition to the hydrodynamic mode below 30 meV (ref. [20]), several new modes emerge. These modes originate from the interband transition in tBLG[25,26]. For tBLG, there exist several van Hove singularities such that the interband plasmons in the long-wave infrared range are to be expected[27]. (We call the modes between 80 and 100 meV and between approximately 100 and 200 meV as low-energy and mid-energy modes, respectively.) The new low-energy interband mode is the focus of our study and is responsible for the realization of a, to our knowledge, new class of chiral Berry plasmons (CBPs) that we present below. Previously, the CBPs were predicted to appear in plasmonic oscillations with the presence of a Hall-like transverse conductivity[24,27], induced by valley polarization in the presence of valley-contrasting Berry curvatures or, equally, by breaking time reversal symmetry (TRS).

The broken inversion symmetry is guaranteed by the intrinsic physical chirality of tBLG. The electron bands in the K and K′ valleys of the original Brillouin zones (BZs) will experience Berry curvatures with equal non-vanishing magnitude but opposite signs as shown in Fig. 2b, right column. As a result, the carriers in each single valley acquire a non-classical transverse velocity due to the Berry curvature, given by $-\frac{e}{\hbar}E\times\int[\mathrm{d}q]f(q)\Omega(q)$[28,29], where e and $\hbar$ are elementary charge and reduced Planck constant, respectively, E is the electric field, f is the Fermi Dirac statistical function and Ω is the Berry curvature. To gain direct insight, we directly calculated the transverse optical conductivity σ_{xy}^{ζ} for the two valleys in the low energy range, where ζ = K or K′ is the valley index. Although the total σ_{xy} is zero, it is non-vanishing in each valley (Fig. 2b, left column). Valley polarized CBP modes may be obtained at an energy corresponding to the non-zero σ_{xy} peak (for example, 80–100 meV). Broken TRS can be fulfilled by using circularly polarized pumping which is free of magnetic field. It is worth mentioning that quarter waveplates as well as circularly polarized light sources in the long-wave infrared range (above 11 μm) are not commonly available. We thus generated a valley polarization excitation by using chiral asymmetric nanoresonators that were circular dichroic. In this study, we designed and fabricated a spiral-shaped plasmonic resonator. Finite-difference time-domain (FDTD) calculations verified that we

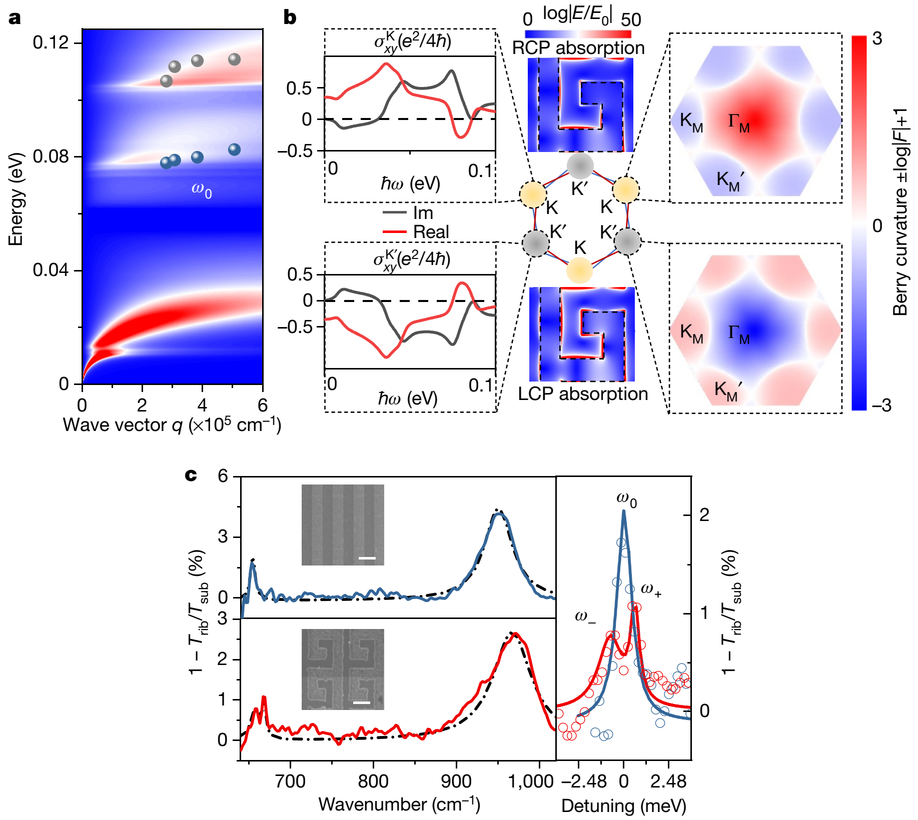

Fig. 2 | Chiral plasmon mode in tBLG. a, The calculated loss function is plotted as a two-dimensional pseudocolour background. Grey and blue dots represent the mid-energy and low-energy plasmon modes, respectively. **b**, Calculated valley-polarized transverse optical conductivity $\sigma_{xy}^{K/K'}$ and Berry curvature in mini-BZs of tBLG. The mini-BZs are schematically marked at the hexagonal BZ corners. Real part (red line) and imaginary part (black line) of the transverse optical conductivity of tBLG with a 1.08° twist angle calculated by the random phase approximation (RPA). The CD of spiral nanoribbons is also shown by the unequal absorption of left-handed circular polarized (LCP) and right-handed circular polarized (RCP) light. **c**, Experimental extinction spectra of the chiral plasmon. A single CBP plasmon peak is observed in the straight nanoribbons (upper left panel). The peak obviously splits into spiral nanoribbons (lower left panel). The lineshapes of the mid-energy plasmon peaks do not change. The blue and red curves are the measured results, the dashed black lines are peak fittings. Inset: scanning electron microscopy images of the nanoribbon structure. Scale bars, 100 nm. Right panel highlights the splitting of the CBP peaks. The open circles are the measured results, the lines are peak fittings.

managed to obtain approximately 11.2% CD in the designed structures, as demonstrated in Fig. 2b (Methods).

Accordingly, a finite Hall-like conductivity and thus CBPs can be expected. We then validated our theoretical expectation by measuring the extinction spectra of the spiral-shaped tBLG resonators. Figure 2c shows the low-energy spectrum of a 120 nm width spiral ribbon array. The results from a straight nanoribbon array are also presented for comparison. Notably, we observe two plasmon peaks at approximately 950 cm^{-1} and 600 cm^{-1}. We also measured samples of varying widths and overlaid the data on the calculated loss function of Fig. 2a. The experiments are in reasonable agreement with the calculated loss function, also confirming the existence of a new interband plasmon mode. More importantly, the low-energy mode obviously splits into two branches in the chiral structures, as compared to Fig. 2c. The splitting is a direct optical signature of the CBPs in nanostructured resonators[27,28,30]. We did not observe a similar behaviour in any of the control samples, including the chiral ribbons made of AB-stacked bilayer graphene (Extended Data Fig. 5).

In particular, the Berry curvature gives rise to a transverse conductivity as demonstrated in Fig. 2b. In pristine tBLG, the opposite Berry curvatures (and σ_{xy}^{ζ}) of the two valleys cancel each other, resulting in zero net σ_{xy}. By contrast, for the chiral ribbon, the light pumping produces an unbalanced carrier density $\rho(k)$ between the two valleys owing to the finite CD. This asymmetric carrier population in the two valleys yields a net transverse conductivity of $\sigma_{xy} = 2e^2/\hbar\int[\mathrm{d}k]\rho(k)\Omega(k)$ (Extended Data Fig. 4). In the presence of a nanoribbon edge, which allows charge to accumulate, the non-zero σ_{xy} results in chiral plasmon edge modes represented by split peaks[27,28]. The observed mode splitting can thus be a measure of the strength of the Berry flux $\int[\mathrm{d}k]\rho(k)\Omega(k)$. Notably, the tBLG platform should enable versatile control of the Berry flux, such as through its electron filling and valley polarization, and their distinct dependences should provide a solid validation of this phenomenon.

First, the valley polarization in our experiment is proportional to the product of CD and incident light power. Even though CD is unchanged for a fixed nanoribbon structure, light power acts as a simple knob to control the Berry flux. Figure 3a summarizes the evolution of the measured plasmon spectra under different light intensities. The largest obtained splitting is about 2 meV, which translates to an effective magnetic field of around 9.5 T (ref. [31]). The energy splitting decreases with light attenuation, which agrees well with the expectation of CBPs.

Second, we studied the plasmons under electrical gating. The spectra mapping as a function of carrier filling of the moiré superlattice is shown in Fig. 3b. Whereas the peak position generally blue shifts with increasing (hole) doping, the peak splitting undergoes a non-monotonic evolution. The plasmon splitting is negligible around a value of the filling factor of $\nu = -n_s/2$. With increasing doping, the plasmon peak splits and the splitting gradually reaches its maximum around a value of the filling factor of $\nu = -3n_s/4$. Beyond this, the energy splitting starts to close on further doping, and merges into a single peak again at a filling factor ν of beyond $-n_s$.

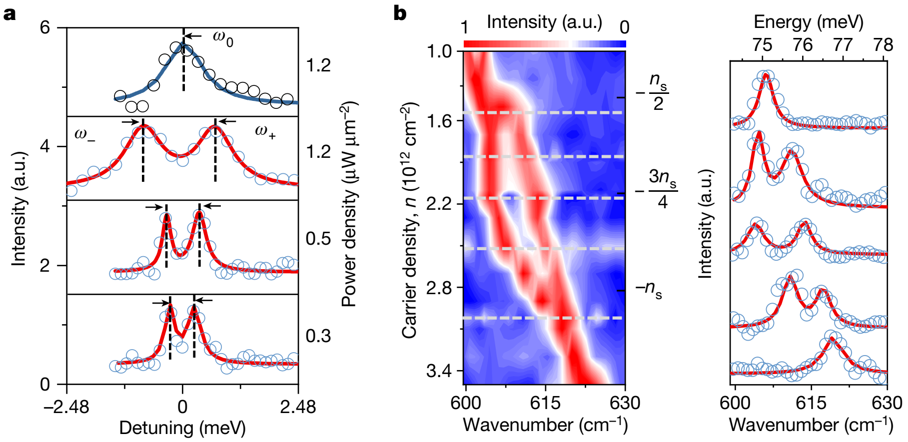

Fig. 3 | Berry flux dependence of CBPs in tBLG. a, Power-dependent extinction spectra of CBPs. A single plasmon peak is observed in straight nanoribbons (the blue curve in the upper panel). The peak obviously splits into spiral nanoribbons (the red curves in the lower panels). The splitting energy increases with incident power density as marked. The open circles are measured results, the lines are peak fittings. Instrument spectral resolution was set as 2 cm^{-1} for 1.2 μW μm^{-2} and 1 cm^{-1} for attenuated light. **b**, Gating-dependent extinction spectra of CBPs. Left: extinction mapping of CBPs as a function of both wavenumber and electrostatic doping. Right: extinction spectra at different electrostatic dopings, selected along the grey dashed lines in the left panel. The open circles are measured results, the lines are peak fittings. The width of the nanoribbon array is 140 nm.

The observed doping-dependent mode splitting can be explained by the influence of electron filling on the Berry curvature of tBLG. The low-energy band structure of the magic-angle tBLG consists of four quasi-flat bands. Two of them are spin-degenerate hole sectors. The four flat bands separately have non-zero Chern number and each valley has opposite Chern number. When the bands are fully filled or fully empty (corresponding to a filling factor of $v = 0$, $-n_s/2$ or $-n_s$), the net Chern number is zero and the valley-polarized Berry curvature is almost vanishing. By contrast, when the bands are half filled (with filling factor $v = -n_s/4$ or $-3n_s/4$), the net Chern number along with the Berry curvature are at a maximum[32,33]. Our observed peak splitting nicely fits this characteristic evolution of the Berry curvature with electron fillings. Hence, the gating experiments further support the existence of the Berry plasmon.

Magnetic-field-free Faraday effect in tBLG

Berry-curvature-induced Faraday-like polarization rotation is another manifestation of the topological CBP. The conventional Faraday effect with a magnetic field has been observed in graphene[34]. The light polarization rotation is determined by

$$\theta_F \approx \mathrm{Re}[\sigma_{xy}]/2c\epsilon_0 \tag{1}$$

where c is the light speed and ϵ_0 is the vacuum dielectric constant. Armed with the anomalous Hall-like conductivity, the CBPs would also naturally produce a Faraday effect, albeit no magnetic field is being applied in this case. Here we demonstrate this effect, showing

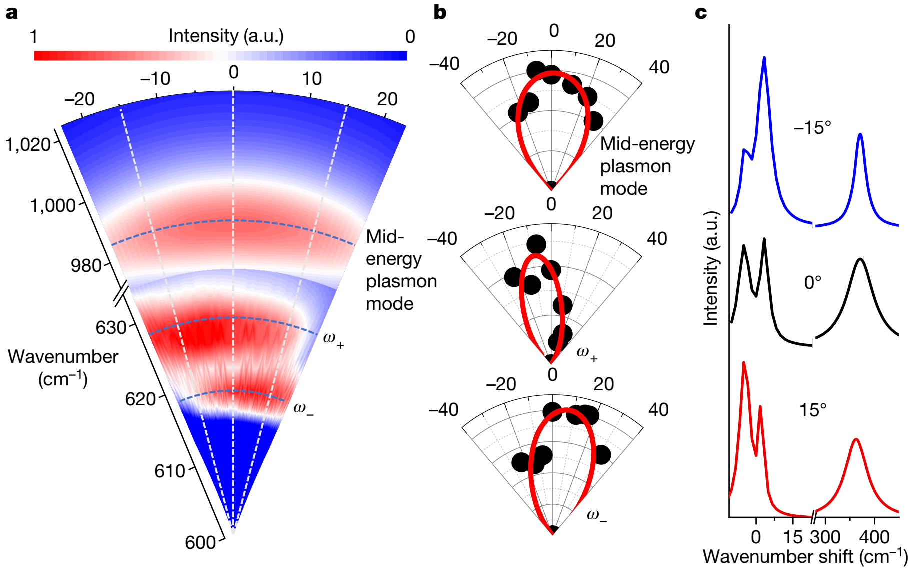

Fig. 4 | Magnetic-field-free Faraday effect of CBPs. a, Extinction mapping of CBPs as a function of both wavenumber and polarization detection angle. The tBLG spiral nanoribbons are excited by a linearly polarized broad-band light source. The incident polarization direction is perpendicular to the long ribbons of the spiral array and defined as 0°. The blue and white dashed lines mark the intensity of different plasmon peaks and extinction spectra at different polarization detection angles. **b**, Plasmon peak intensity as a function of the polarization detection angle, selected along the blue dashed lines in **a**. The polarization of the mid-energy plasmon aligns with the incident light. The polarization of the split CBP plasmon peaks (ω_+ and ω_-) rotate oppositely. The solid lines are fitted curves using a $\cos^2\alpha$ function (α denotes the angle between the incident polarization and the polarization detection angle). **c**, Fitted peak curves of extinction spectra at different polarization detection angles, selected along the white dashed lines in **a**.

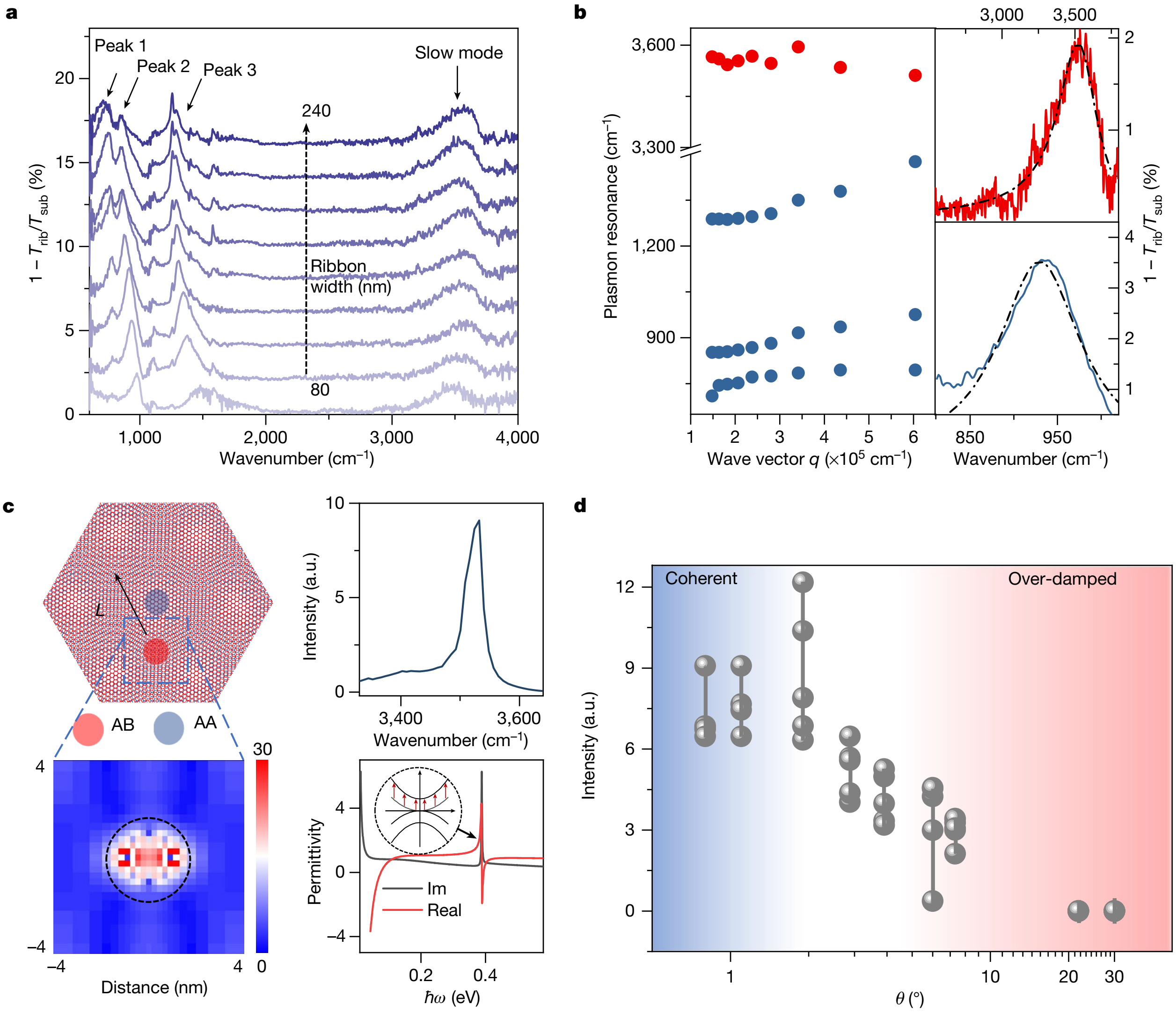

Fig. 5 | Slow plasmon mode in tBLG. **a**, Extinction spectra of tBLG ribbons on a SiO_2 substrate with different ribbon widths. The spectra are vertically displaced for clarity. The mid-energy plasmon mode splits into three branches (marked by peaks 1, 2 and 3) owing to its interaction with substrate SO phonons. A dispersionless mode (around 3,500 cm^{-1}) emerges and is indicated by the slow mode. **b**, Plasmon frequency as a function of the wave vector for the peaks in **a**. Fano and Lorentz resonances are obtained for the slow mode and mid-energy plasmon mode, respectively (right panel, ribbon width 120 nm). Red and blue curves are measured results, dashed lines are fitting curves. The Fano coupling constant $q = -8$. **c**, Schematic of the origin of the slow plasmon mode. Upper left panel: the moiré pattern as seen in tBLG. A simplified model shows the AA-stacked and AB-stacked domains as well as the domain boundary regions in between. The slow plasmon arises from the localized γ-mode plasmon of the isolated AB-stacked disks. Upper right panel: plot of extinction spectrum of the high-energy plasmonic resonance. Lower right panel: the calculated dielectric function of AB-stacked graphene indicates its metallic nature at approximately 0.4 eV. Inset: the four lowest non-interacting ground-state electronic bands of AB-stacked graphene. An interlayer absorption around 0.4 eV is marked. Lower left panel: electric field-enhancement in real space. The AB-stacked bilayer region is marked by the dashed circle. **d**, Statistics of the measured extinction spectral weights as a function of the twist angle. Grey dots in one column represent devices with different ribbon widths. The plasmon turns from a coherent regime (blue) to an over-damped regime (red) with increasing twist angle.

significant polarization rotation consistent with a magnetic field of order 10 T. Extended Data Figure 6 describes the experimental setup. Figure 4a shows the extinction mapping of the chiral plasmon mode as a function of both wavenumber and the polarization detection angle. Although the polarization of the mid-energy mode with negligible σ_{xy} does not change, those of the two CBP edge modes ω_+ and ω_- obviously rotate. To clearly see this rotation, we summarize the spectral intensity evolution of the three modes as polar plots in Fig. 4b. The edge modes ω_+ and ω_- rotate the input polarization by about +15° and −15°, respectively. These spectra at different angles are also compared in Fig. 4c. It is worth mentioning that this magnetic-field-free Faraday rotation is quite efficient owing to the plasmonic enhancement. Such a large rotation angle in the conventional Faraday effect would require a large magnetic field up of to 7 T (ref. [34]). Finally, as shown in Extended Data Fig. 7, the Faraday angles are opposite between the mirrored configurations, which matches our expectation and supports the topological origins of CBPs.

Slow plasmon mode in tBLG

We proceed to discuss plasmonics in the high-energy spectral range. Figure 5a shows the extinction spectra of tBLG nanoribbons on the SiO_2 substrate with widths ranging from 80 to 240 nm, demonstrating three peaks in the mid-energy range (<0.2 eV) and a high-energy peak at around 0.4 eV or 3,500 cm^{-1}. The former three peaks (marked as peaks 1, 2 and 3 in Fig. 5a) come from the mid-energy interband plasmons coupled to the surface phonons of the SiO_2 substrate[20], whereas the latter high-energy peak is a new plasmon mode. It exhibits two unique features. First, its energy–momentum dispersion (see Methods for details) is nearly flat, as shown in Fig. 5b. We thus called this peak a slow mode because its group velocity ($v_g = \frac{d\omega}{dk} = \frac{dE}{\hbar dk}$) approaches zero. Second, the peaks of the slow mode present with a strongly asymmetric Fano lineshape. In comparison, a plasmon commonly shows a quasi-Lorentzian peak. (More precisely, plasmon peaks approaching the surface phonon frequency on a SiO_2 substrate are slightly Fano-like, because they are phonon–plasmon hybrid states.) The resonance energy and asymmetric lineshape indicate that this high-energy slow mode is due to the so-called γ-mode plasmon in AB-stacked bilayer graphene[30]. In particular, this mode arises from an interband resonant absorption approximately 0.4 eV (as illustrated in Fig. 5c, inset). The γ-mode has been predicted to be a Fano oscillator around 3,500 cm^{-1}. The Fano feature is produced by interference between the discrete interband resonant absorption and the plasmon oscillation, and agrees well with the measurements[30]. At the same time, theoretical calculation of the loss function (Extended Data Fig. 8) also indicate that, at a moderate doping level (around 2×10^{12} cm^{-2}), the γ-mode is almost dispersionless.

We propose a localized plasmon model to explain the experimental findings. As shown in Fig. 5c, at small twist angles (<2°), regions of the tBLG lattice are relaxed into triangular AB-stacked bilayer graphene domains[12,35]. The calculated dielectric function of the AB graphene and tBLG indicates that, at this spectral range, the former is metallic whereas the latter is insulating (Fig. 5c). Hence, the γ-mode plasmon of the AB domain should be strongly localized. Using the calculated dielectric constants, we numerically calculated the local electric field distribution in real space by FDTD calculations. Figure 5c shows the local electric field enhancement around the AB-stacked centre. In addition, the calculated extinction spectra also show a Fano-shaped localized surface plasmon resonance peaked at around 3,530 cm^{-1}. For larger twist angles, these AB domains are not formed within the moiré lattice as the energetics of AB lattice relaxation become unfavourable, with the phase transition predicted to be approximately 6° (ref. [35]). We examined the high-energy plasmon in tBLG under different twist angles θ ($\theta = 0.8°$, 1.9°, 2.88°, 3.9°, 6°, 7.3°, 21.8°, 30°(AB-stacked)). Figure 5d summarizes the slow plasmon spectral weight as a function of θ. With increasing twist angle, the reducing AB domain in each moiré superlattice leads to a damped modal intensity (see Extended Data Fig. 9 for a typical spectra set of 7.3°, showing a weakened γ-mode). The evolution is fully consistent with our physical picture.

Finally, we should highlight the practical significance of the observed Berry plasmon and slow plasmon. The CBPs we discussed can be used as an experimental probe for optic monitoring of the Berry flux, which is a fundamentally useful non-invasive way to study topological materials. In practice, the demonstrated tuneable CBPs also enable numerous intriguing nanophotonic devices, such as magnetic-field-free Faraday rotators and unidirectional waveguide. In addition, the mid-infrared range contains two ambient transparency windows. Although graphene plasmonic devices have been extensively studied in the 8–12 μm range[6,36–38], light–matter interactions in the 3–5 μm range always suffer from fundamental damping and phonon scattering processes. Our discovery of the slow plasmon mode should offer a new way to access plasmonics in this highly sought after spectral window for new infrared devices[37,39,40]. Moving forward, a microscopic model beyond our phenomenological theory in conjunction with nano-imaging may deepen current understanding and help to explore other purely intrinsic properties of tBLG plasmonics.

Online content

Any methods, additional references, Nature Research reporting summaries, source data, extended data, supplementary information, acknowledgements, peer review information; details of author contributions and competing interests; and statements of data and code availability are available at https://doi.org/10.1038/s41586-022-04520-8.

1. Cao, Y. et al. Correlated insulator behaviour at half-filling in magic-angle graphene superlattices. *Nature* **556**, 80–84 (2018).
2. Cao, Y. et al. Unconventional superconductivity in magic-angle graphene superlattices. *Nature* **556**, 43–50 (2018).
3. Hesp, N. C. H. et al. Observation of interband collective excitations in twisted bilayer graphene. *Nat. Phys.* **17**, 1162–1168 (2021).
4. Hu, F. et al. Real-space imaging of the tailored plasmons in twisted bilayer graphene. *Phys. Rev. Lett.* **119**, 247402 (2017).
5. Sunku, S. S. et al. Photonic crystals for nano-light in moire graphene superlattices. *Science* **362**, 1153–1156 (2018).
6. Ni, G. X. et al. Plasmons in graphene moiré superlattices. *Nat. Mater.* **14**, 1217–1222 (2015).
7. Brey, L., Stauber, T., Slipchenko, T. & Martín-Moreno, L. Plasmonic Dirac cone in twisted bilayer graphene. *Phys. Rev. Lett.* **125**, 256804 (2020).
8. Jalali, B. et al. Prospects for silicon mid-IR Raman lasers. *IEEE J. Sel. Top. Quantum Electron.* **12**, 1618–1627 (2006).
9. Wong, D. et al. Cascade of electronic transitions in magic-angle twisted bilayer graphene. *Nature* **582**, 198–202 (2020).
10. Choi, Y. et al. Correlation-driven topological phases in magic-angle twisted bilayer graphene. *Nature* **589**, 536–541 (2021).
11. Choi, Y. et al. Electronic correlations in twisted bilayer graphene near the magic angle. *Nat. Phys.* **15**, 1174–1180 (2019).
12. Yoo, H. et al. Atomic and electronic reconstruction at the van der Waals interface in twisted bilayer graphene. *Nat. Mater.* **18**, 448–453 (2019).
13. Stauber, T., Low, T. & Gomez-Santos, G. Chiral response of twisted bilayer graphene. *Phys. Rev. Lett.* **120**, 6 (2018).
14. Brown, R., Walet, N. R. & Guinea, F. Edge modes and nonlocal conductance in graphene superlattices. *Phys. Rev. Lett.* **120**, 026802 (2018).
15. Guinea, F. & Walet, N. R. Continuum models for twisted bilayer graphene: effect of lattice deformation and hopping parameters. *Phys. Rev. B* **99**, 205134 (2019).
16. Cea, T., Walet, N. R. & Guinea, F. Electronic band structure and pinning of Fermi energy to Van Hove singularities in twisted bilayer graphene: A self-consistent approach. *Phys. Rev. B* **100**, 205113 (2019).
17. Lin, X. et al. Chiral plasmons with twisted atomic bilayers. *Phys. Rev. Lett.* **125**, 077401 (2020).
18. Fei, Z. et al. Gate-tuning of graphene plasmons revealed by infrared nano-imaging. *Nature* **487**, 82–85 (2012).
19. Koppens, F. H. L., Chang, D. E. & de Abajo, F. J. G. Graphene plasmonics: a platform for strong light-matter interactions. *Nano Lett.* **11**, 3370–3377 (2011).
20. Yan, H. et al. Damping pathways of mid-infrared plasmons in graphene nanostructures. *Nat. Photonics* **7**, 394–399 (2013).
21. Ju, L. et al. Graphene plasmonics for tunable terahertz metamaterials. *Nat. Nanotechnol.* **6**, 630–634 (2011).
22. Carozo, V. et al. Raman signature of graphene superlattices. *Nano Lett.* **11**, 4527–4534 (2011).
23. Zhu, H. et al. Observation of chiral phonons. *Science* **359**, 579–582 (2018).
24. Kim, C.-J. et al. Chiral atomically thin films. *Nat. Nanotechnol.* **11**, 520–524 (2016).
25. Stauber, T., San-Jose, P. & Brey, L. Optical conductivity, Drude weight and plasmons in twisted graphene bilayers. *New J. Phys.* **15**, 113050 (2013).
26. Stauber, T. & Kohler, H. Quasi-flat plasmonic bands in twisted bilayer graphene. *Nano Lett.* **16**, 6844–6849 (2016).
27. Song, J. C. W. & Rudner, M. S. Chiral plasmons without magnetic field. *Proc. Natl Acad. Sci.* **113**, 4658–4663 (2016).
28. Kumar, A. et al. Chiral plasmon in gapped Dirac systems. *Phys. Rev. B* **93** (2016).
29. Yao, W. & Niu, Q. Berry phase effect on the exciton transport and on the exciton Bose-Einstein condensate. *Phys. Rev. Lett.* **101**, 106401 (2008).
30. Low, T., Guinea, F., Yan, H., Xia, F. & Avouris, P. Novel midinfrared plasmonic properties of bilayer graphene. *Phys. Rev. Lett.* **112**, 116801 (2014).
31. Yan, H. et al. Infrared spectroscopy of tunable Dirac terahertz magneto-plasmons in graphene. *Nano Lett.* **12**, 3766–3771 (2012).
32. Nuckolls, K. P. et al. Strongly correlated Chern insulators in magic-angle twisted bilayer graphene. *Nature* **588**, 610–615 (2020).
33. Serlin, M. et al. Intrinsic quantized anomalous Hall effect in a moiré heterostructure. *Science* **367**, 900 (2020).
34. Crassee, I. et al. Giant Faraday rotation in single- and multilayer graphene. *Nat. Phys.* **7**, 48–51 (2011).
35. Nam, N. N. T. & Koshino, M. Lattice relaxation and energy band modulation in twisted bilayer graphene. *Phys. Rev. B* **96**, 075311 (2017).
36. Ni, G. X. et al. Ultrafast optical switching of infrared plasmon polaritons in high-mobility graphene. *Nat. Photon.* **10**, 244–247 (2016).
37. Ni, G. X. et al. Fundamental limits to graphene plasmonics. *Nature* **557**, 530–533 (2018).
38. Chen, J. et al. Optical nano-imaging of gate-tunable graphene plasmons. *Nature* **487**, 77–81 (2012).
39. Koppens, F. H. L. et al. Photodetectors based on graphene, other two-dimensional materials and hybrid systems. *Nat. Nanotechnol.* **9**, 780–793 (2014).
40. Alonso-González, P. et al. Controlling graphene plasmons with resonant metal antennas and spatial conductivity patterns. *Science* **344**, 1369–1373 (2014).

Methods

tBLG sample preparation

Samples were prepared by a ‘tear-and-stack’ method[41] from a large-area, single-crystalline graphene. Graphene was grown by a CVD method on copper foil[42] and transferred to SiO_2/silicon substrates. Then, a ‘polyvinyl alcohol (PVA) stamp’ stacked with polydimethylsiloxane and PVA was prepared on a glass slide. Through a transfer station, the ‘PVA stamp’ was aligned with the middle of the hexagonal graphene flake and half of it picked up by heating the PVA at 80 °C. The remaining part of the graphene on SiO_2 was rotated by commensurable angles and then slowly placed in contact with the part on the PVA. The two parts were maintained in close contact for 8 h to flatten the contact surface. The sample was then released onto the substrate by immersing in water to dissolve the PVA. Finally, the samples were annealed in argon gas for 12 h at 350 °C. The as-prepared sample was characterized by a homemade micro-Raman spectrometer equipped with a 514 nm laser. As summarized in Fig. 1c inset, the R' peak starts with an elastic scattering of photon-generated electrons caused by the periodic moiré potential. The electron momentum is scattered by q corresponding to the rotation between the top and bottom BZs during this process. Subsequently, the electrons are inelastically scattered back by the phonon and recombine with the holes. An efficient momentum transfer q, or highly ordered moiré superlattice in real space, is essential for this Raman emission. The plasmonic resonators were pattern by an electron-beam lithography system (Raith EBPG5200) and etched in an inductively coupled plasma etching system (Oxford Instrument).

FTIR measurements

The fabricated nanoribbons were designed to have the same widths as the spacing in the vicinity of ribbons, corresponding to a filling factor of 50%. Each nanoresonator array was 50 × 50 μm^2. Broadband transmission measurements were performed with a micro FTIR spectrometer (Bruker VERTEX 80V equipped with a Hyperion microscope). The electromagnetic responses of the tBLG nanoresonators were demonstrated from the extinction spectra $1 - T_{\mathrm{rib}}/T_{\mathrm{sub}}$, where T_{rib} and T_{rib} are the transmissions through the ribbon regime and substructure regime without tBLG, respectively. All the plasmon peaks discussed in the main Article have also been double-checked by polarized extinction spectra to preclude interferences from background and chemical contamination. In this method, we first recorded the transmission signal T_{per} for light perpendicularly polarized with respect to the ribbons or the long axis of the spiral ribbons. Then the signal T_{par} for light parallelly polarized was also measured. On the basis of the fact that only perpendicularly polarized light is able to efficiently launch a plasmon signal but the interferences are nearly polarization independent for the same ribbon array, the extinction spectrum $1 - T_{\mathrm{per}}/T_{\mathrm{par}}$ largely cancels out all the interference. In extracting the energy–momentum dispersion, the wave vector of the nanoresonator is calculated as $q = \pi/(W_e)$ and the corrected ribbon width as $W_e = W - W_0$ ($W_0 \approx 30$ nm is a modified constant). Doping-dependent measurements were performed by fabricating electrodes on a chiral nanoribbon array and varying the gate voltages.

Band structure and random phase approximation calculation

In the tBLG system, the electronic band structure can be well described by an effective continuum model because the moiré period is much larger than the lattice constant of graphene[43–45]. Here we assume the following form for the Hamiltonian:

$$H^{\zeta} = H_0^{\zeta} + H_1^{\zeta} + H_2^{\zeta}$$

where $\zeta = \pm 1$ is the valley index. H_0^{ζ} represents the Hamiltonian of pristine tBLG in wave vector (**k**) space and is given by:

$$H_0^{\zeta} = \begin{bmatrix} -\hbar v_{\mathrm{F}} R\left(\frac{\theta}{2}\right)(\mathbf{k} - \mathbf{K}_1^{\zeta})\bullet(\zeta\sigma_x, \sigma_y) & U_{\zeta}^{+}(r) \\ U_{\zeta}(r) & -\hbar v_{\mathrm{F}} R\left(-\frac{\theta}{2}\right)(\mathbf{k} - \mathbf{K}_2^{\zeta})\bullet(\zeta\sigma_x, \sigma_y) \end{bmatrix},$$

where $\sigma_{x,y}$ are the Pauli matrices, $R(\theta)$ presents the rotation by θ, $\frac{\hbar v_{\mathrm{F}}}{a} = 2.1354\,\mathrm{eV}$, $a = 2.46$ Å is the graphene lattice size, and $\mathbf{K}_{1,2}^{\zeta} = -\frac{\zeta 4\pi}{3a} R\left(\mp\frac{\theta}{2}\right)\begin{bmatrix} 1 \\ 0 \end{bmatrix}$ is the location of graphene's Dirac points. The interlayer coupling U_{ζ} is given by:

$$U_{\zeta} = \begin{bmatrix} u & u' \\ u' & u \end{bmatrix} + \begin{bmatrix} u & u'\mathrm{e}^{-\mathrm{i}\zeta 2\pi/3} \\ u'\mathrm{e}^{\mathrm{i}\zeta 2\pi/3} & u \end{bmatrix}\mathrm{e}^{\mathrm{i}\zeta \mathbf{G}_1 \bullet \boldsymbol{r}} + \begin{bmatrix} u & u'\mathrm{e}^{\mathrm{i}\zeta 2\pi/3} \\ u'\mathrm{e}^{-\mathrm{i}\zeta 2\pi/3} & u \end{bmatrix}\mathrm{e}^{\mathrm{i}\zeta (\mathbf{G}_1 + \mathbf{G}_2)\bullet \mathbf{r}}.$$

We assume that the diagonal amplitude $u = 75\,\mathrm{meV}$ and the off-diagonal amplitude $u' = 97.5$ meV (ref. [46]). The reciprocal lattice vectors for the moiré pattern are given by $\mathbf{G}_1 = -\frac{2\pi}{\sqrt{3}L_{\mathrm{m}}}\begin{bmatrix} 1 \\ \sqrt{3} \end{bmatrix}$ and $\mathbf{G}_2 = \frac{4\pi}{\sqrt{3}L_{\mathrm{m}}}\begin{bmatrix} 1 \\ 0 \end{bmatrix}$, where $L_{\mathrm{m}} = a/2\sin(\frac{\theta}{2})$ is the moiré lattice constant. **r** is the Bloch wave vector in the moiré BZ.

H_1^{ζ} is the mass term that breaks the sublattice symmetry in both graphene layers, while preserving the inversion symmetry of the twisted bilayer graphene The effective Hamiltonian model for tBLG does not account for the finite regions of relaxed AB domains. We break the inversion symmetry in the continuum model by introducing a mass term:

$$H_1^{\zeta} = \begin{bmatrix} \Delta\sigma_z & 0 \\ 0 & -\Delta\sigma_z \end{bmatrix}$$

where Δ is the staggered sublattice potential exerted on each graphene layer.

H_2^{ζ} is the valley polarization term given by:

$$H_2^{\zeta} = \begin{bmatrix} \zeta\Delta_{\mathrm{v}} I & 0 \\ 0 & \zeta\Delta_{\mathrm{v}} I \end{bmatrix}$$

where Δ_{v} is the valley polarization energy and I is the 2 × 2 identity matrix.

We next calculate the conductivity of tBLG using the Kubo formula:

$$\sigma_{\alpha,\beta}^{\zeta} = \frac{-ie^2\hbar}{\pi^2}\int \mathrm{d}^2\mathbf{k} \sum\nolimits_{n,m} \frac{f(\epsilon_{mk}^{\zeta}) - f(\epsilon_{nk}^{\zeta})}{\epsilon_{mk}^{\zeta} - \epsilon_{nk}^{\zeta}} \frac{\langle mk|v_{\alpha}^{\zeta}|nk\rangle\langle nk|v_{\beta}^{\zeta}|mk\rangle}{\epsilon_{mk}^{\zeta} - \epsilon_{nk}^{\zeta} + \hbar\omega + i\eta}$$

where $v_{\alpha,\beta} = \partial H^{\zeta}/\partial k_{\alpha,\beta}$ and $\alpha, \beta \in \{x, y\}$. $f(\cdot)$ is the Fermi function and ϵ_{nk}^{ζ} and $|nk\rangle$ denote the eigenenergy and eigenfunction of H^{ζ}. An infinitesimal increment $i\eta$ is included to ensure convergence. Throughout this work we assume that $T = 300$ K, $\theta = 1.08^{\circ}$, $\Delta = 10$–40 meV (ref. [47]), $\Delta_{\mathrm{v}} = 10$ meV and $\eta = 0.5$ meV. With different Δ, the calculated results are only slightly changed and qualitatively similar. $\Delta = 40$ meV gives the loss function that is best fitted to the measurements. Given H^{ζ} for both valleys, we fine tune the chemical potential so that the carrier concentration in the sample is $-2 \times 10^{12}\,\mathrm{cm}^{-2}$.

The dielectric function of tBLG can be obtained by a current continuity through $\varepsilon_{\mathrm{RPA}}(q, \omega) = 1 + \frac{\mathrm{i}}{2\varepsilon_0\varepsilon}\frac{|q|}{\omega}\sigma_{xx}(\omega)$, where q, ω, ε_0 and ε are the momentum, frequency, permittivity of free space and relative permittivity of SiO_2, respectively.

The Berry curvature F of the flat bands for one valley ξ is given by

$$F^{\xi} = \nabla \times A^{\xi}$$

Here A^{ξ} is the Abelian Berry connection

$$A^{\xi} = \mathrm{i}\langle mk^{\xi}|\partial_{\mathbf{k}}|n\mathbf{k}^{\xi}\rangle,$$

where $|nk\rangle$ denotes the eigenfunction of H^{ζ}.

FDTD calculation

Numerical simulations were performed using commercial software, FDTD Solutions v.8.15 (Lumerical Solutions). In the simulations, the chiral bilayer graphene nanostructures were modelled as two-dimensional structures in free space. A normally incident, linearly polarized plane wave in the wavelength range from 10 to 20 μm was launched onto the chiral bilayer graphene nanostructure to simulate a propagating linearly polarized plane wave interacting with the nanostructure. To simulate the interaction of a propagating left-handed circularly polarized or right-handed circularly polarized plane wave with the nanostructure, two plane waves with orthogonal linear polarizations and a phase difference of −π/2 or π/2 were launched onto the nanostructure unit. Periodic boundary conditions and perfect matching layers were applied at the boundaries parallel and perpendicular to the direction of wave propagation, respectively. The bilayer graphene was simulated as a two-dimensional material characterized using surface conductivity by the graphene material model in FDTD calculations[48,49], where a scattering rate of 0.001 eV, a chemical potential of 0.05 eV and a temperature of 300 K were used. The complex electric and magnetic fields were extracted from the surface of the structure. The optical chirality is defined as

$$\mathrm{CD} = -\frac{\varepsilon_0\omega}{2}\mathrm{Im}[\widetilde{\mathbf{E}}^{*}\boldsymbol{\cdot}\widetilde{\mathbf{B}}],$$

where ε_0 is the permittivity of free space, ω is the angular frequency of light, $\widetilde{\mathbf{E}}^{*}$ represents the conjugation of the complex electric field and $\widetilde{\mathbf{B}}$ denotes the complex magnetic field. The optical chirality of circularly polarized light (CPL) in free space is obtained as $C_{\mathrm{CPL}} = \pm\frac{\varepsilon_0\omega}{2c}E_{\mathrm{CPL}}$, where c and E_{CPL} are the speed of light in free space and the electric field amplitude of CPL, respectively. Therefore, the optical chirality enhancement $\hat{C}$ can be described as

$$\hat{C} = \frac{C}{|C_{\mathrm{CPL}}|} = -\frac{c\mathrm{Im}[\widetilde{\mathbf{E}}^{*}\boldsymbol{\cdot}\widetilde{\mathbf{B}}]}{|E_{\mathrm{CPL}}|^2}$$

It should be noted that it is challenging to obtain the exact field distributions for the two split CBP edge modes, as in the FDTD calculation it is difficult to take the Berry curvature effect into account. Hence, the calculation only uses the modelled σ_{xx} of tBLG, without considering the σ_{xy} (modification of the dielectric properties of the tBLG by the Berry curvature). Despite this, we believe the calculation largely reflects the CD as it is not large.

Peak fittings

To more clearly distinguish the resonant peaks from background noise, we fitted the experimental results to different oscillator models. For conventional graphene plasmons, we used the Lorentz formula $y = y_0 + \frac{2A}{\pi}\frac{w}{4(x-x_c)^2+w^2}$, where y_0 is the offset of the fitting curve, x_c is the centre point, w is the line width and A denotes the curve area. For the chiral plasmon mode, peak analysis was undertaken by fitting the experimental data with a sum of several Lorentz-shaped curves. For the slow plasmon mode, we used the Fano formula $\sigma = r\frac{(\beta+q)^2}{\beta^2+1}$, where $\beta = 2(\omega-\omega_0)/\gamma$ denotes the linewidth, q is the critical Fano coupling constant, r is the corrected parameter and ω is the Fano peak position, to fit the experimental slow plasmon curves in the spectra.

In the fitting process, ordinary least squares was applied to pick an array of variables by the principle of minimizing the square sum of differences between the series of points on the fitting curves and the experimental curves.

Data availability

The data that support Figs. 1–5 and the Extended Data figures can be found in the source data. Source data are provided with this paper.

Code availability

The codes that were used in this study are available from the corresponding authors upon reasonable request.

41. Kim, K. et al. Van der Waals heterostructures with high accuracy rotational alignment. *Nano Lett.* **16**, 1989–1995 (2016).
42. Li, X. S. et al. Large-area synthesis of high-quality and uniform graphene films on copper foils. *Science* **324**, 1312–1314 (2009).
43. Bistritzer, R. & MacDonald, A. H. Moire bands in twisted double-layer graphene. *Proc. Natl Acad. Sci. USA* **108**, 12233–12237 (2011).
44. Lopes dos Santos, J. M. B., Peres, N. M. R. & Castro Neto, A. H. Continuum model of the twisted graphene bilayer. *Phys. Rev. B* **86**, 155449 (2012).
45. Moon, P. & Koshino, M. Optical absorption in twisted bilayer graphene. *Phys. Rev. B* **87**, 205404 (2013).
46. Koshino, M. et al. Maximally localized Wannier orbitals and the extended Hubbard model for twisted bilayer graphene. *Phys. Rev. X* **8**, 031087 (2018).
47. Liu, J. & Dai, X. Theories for the correlated insulating states and quantum anomalous Hall effect phenomena in twisted bilayer graphene. *Phys. Rev. B* **103**, 035427 (2021).
48. Hanson, G. Dyadic Green's functions and guided surface waves for a surface conductivity model of graphene. *J. Appl. Phys.* **103**, 064302 (2008).
49. Stauber, T., Low, T. & Gomez-Santos, G. Plasmon-enhanced near-field chirality in twisted van der Waals heterostructures. *Nano Lett.* **20**, 8711–8718 (2020).

Acknowledgements This project was primarily supported by the National Key R&D Program of China (2018YFA0307300, 2018YFA0209100 and 2017YFA0206301), the National Natural Science Foundation of China (61934004 and 62005119), the Program for High-Level Entrepreneurial and Innovative Talent Introduction of Jiangsu Province, the Strategic Priority Research Program of the Chinese Academy of Sciences (grant no. XDB30000000) and the Fundamental Research Funds for the Central Universities. X.L acknowledges the Shenzhen Science and Technology Program (No. (2021)105). L.S. acknowledges financial support from the National Natural Science Foundation of China (NSAF, U1930402) and computational resources from the Beijing Computational Science Research Center. We also thank the NJU micro-fabrication and integration centre for support.

Author contributions X.W. conceived the project. T.H., B.Z. and J.W. fabricated and measured the samples. X.T. carried out the electron beam lithography. C.S. and X.L. grew the graphene single crystals. H.W. and L.S. performed the FDTD calculations. K.K., S.H.P., T.L., Z.L., T.Y. and Z.Z. performed the band structure and random phase approximation calculation. B.Z. helped perform scanning electron microscopy and contributed to the data processing. X.W. and T.H. analysed the data and wrote the manuscript. X.W., Y.S., T.L. and X.L. supervised the research. All authors discussed the results obtained.

Competing interests The authors declare no competing interests.

Additional information

Correspondence and requests for materials should be addressed to Xuesong Li, Tony Low, Yi Shi or Xiaomu Wang.

Peer review information *Nature* thanks Pablo Alonso-González, Alexander McLeod and the other, anonymous, reviewer(s) for their contribution to the peer review of this work.

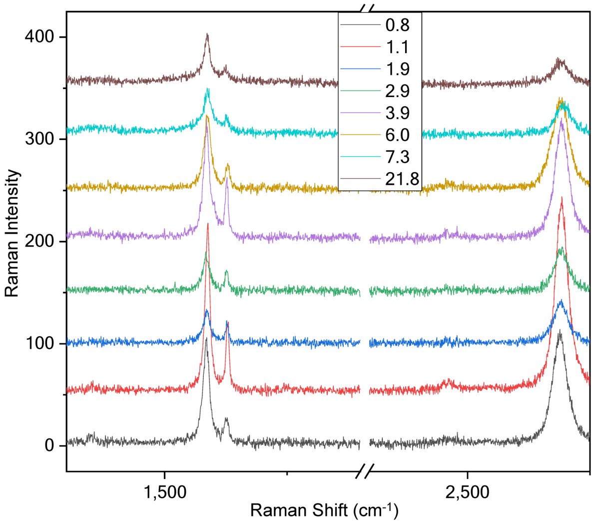

Extended Data Fig. 1 | Raman spectra of tBLG samples. R′ peaks are observed in all samples from 0.8 to 21.8 degree.

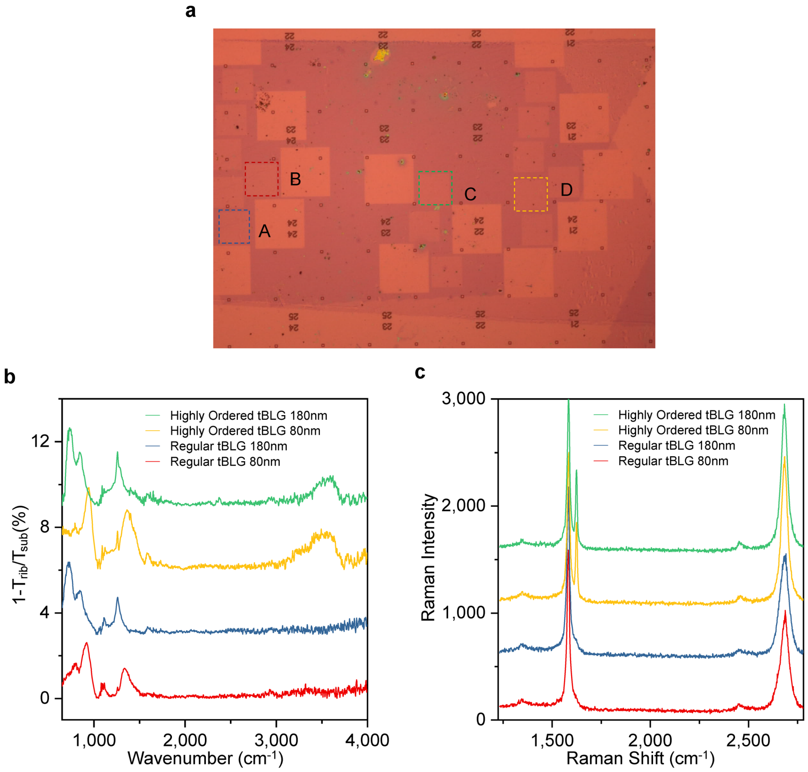

Extended Data Fig. 2 | Comparison between highly ordered and regular tBLGs. a, Optical photo image of the 2.88°tBLG sample showing in Fig. 1b after nano-ribbon fabrication. **b**, Extinction spectra of the marked regions A (blue) B (red) C (green) D (yellow) in (a). **c**, Raman spectra of the marked regions A B C D in (a). The regions A and B (C and D) are regular (highly ordered) tBLG defined due to the absence (presence) of R′ Raman peak. The non-trivial plasmon mode can be only observed in samples with R′ peak, indicating the key roles played by ordered moiré superlattice.

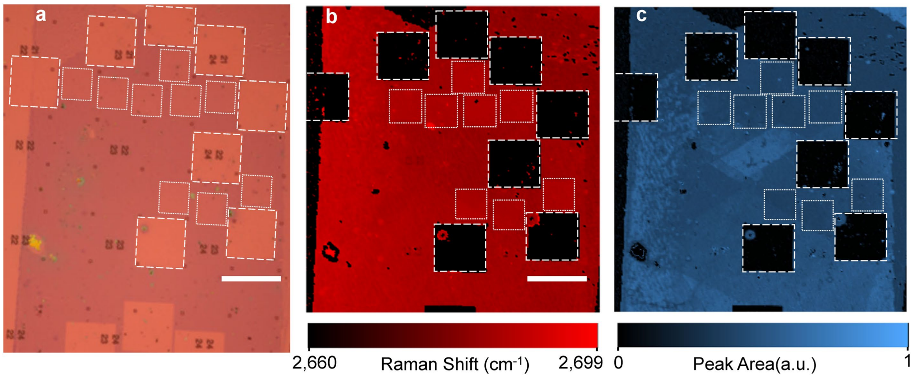

Extended Data Fig. 3 | Characterization of twisted bilayer graphene. **a**, Optical microscope image of a tBLG sample after fabricating nanoribbons. The nano-ribbon region and fully etched background region are marked by dotted and dashed boxes, respectively. Scale bar 100 μm. **b, c**, Raman position (b) and area (c) mapping of 2D peak of the sample in (a).

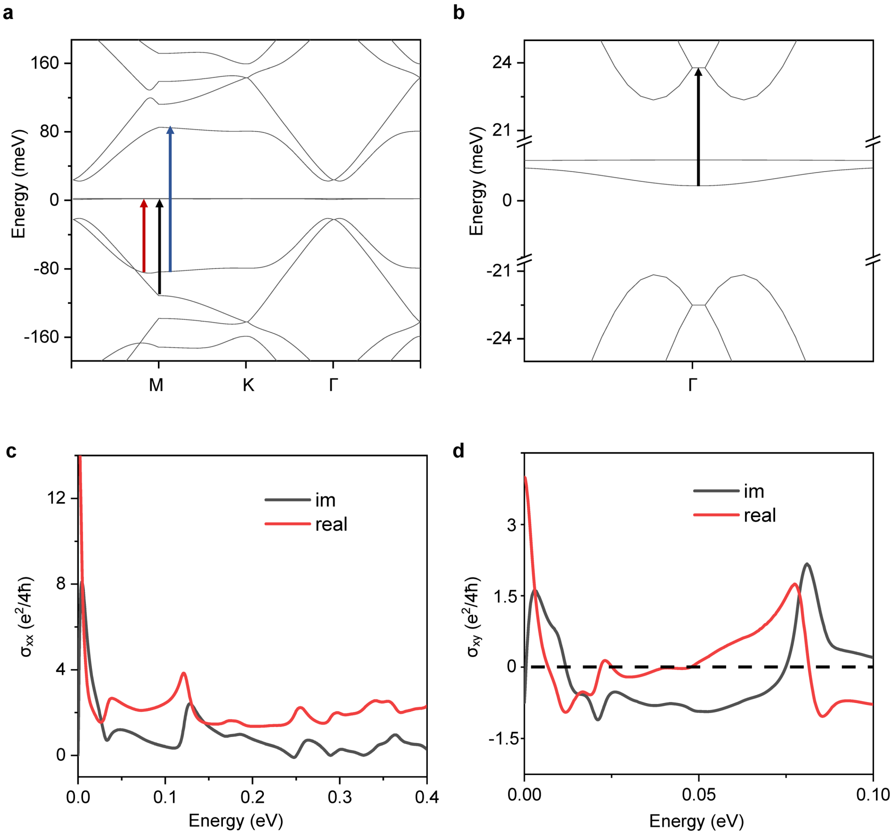

Extended Data Fig. 4 | Band structure and RPA calculation. a, Calculated band structure of tBLG modeled by a continuum model. **b**, Corresponding low energy band structure in (a). The red, black and blue arrows indicate interband transition between multiple van Hove singularities with energy of 0.08 eV, 0.11 eV and 0.16 eV. **c, d**, Calculated longitude (c) and transverse (d) optical conductivity of tBLG. Grey and red curves represent imaginary and real part, respectively.

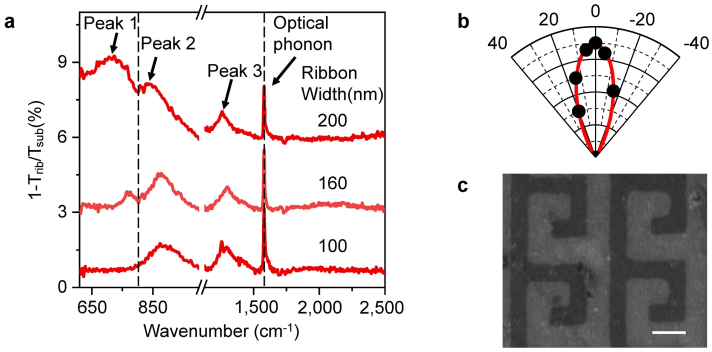

Extended Data Fig. 5 | Plasmon mode in AB stacked bilayer graphene. **a**, Extinction spectra of AB stacked bilayer graphene. Graphene flake is patterned to spiral nanoribbon arrays whose width ranges from 100 to 200 nm. The three branches of mid-energy plasmon are marked. The dashed lines indicate silica SO phonon and graphene optical phonon, respectively. **b**, Plasmon peak (peak 1 of the 200 nm sample) intensity as a function of the polarization detection angle. **c**, SEM image of a typical spiral nanoribbon made of AB stacked graphene. Scale bar 200 nm.

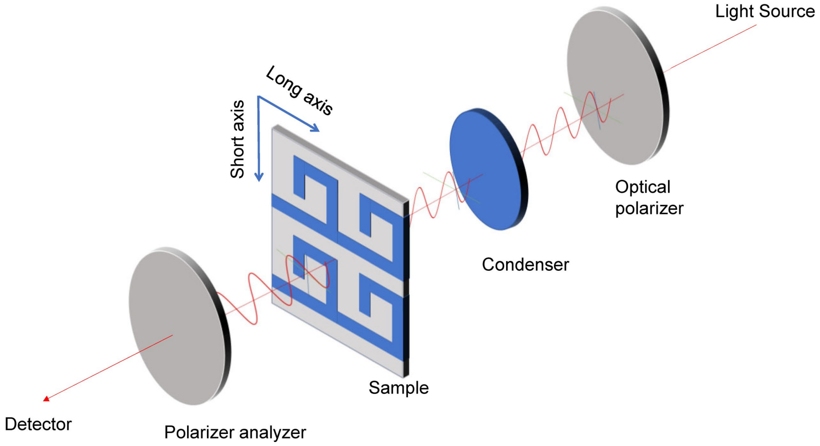

Extended Data Fig. 6 | Schematic of experimental setup for magnetic field-free Faraday effect measurements. The incident IR source is linearly polarized, aligning with the short axes of the spiral ribbons, and a polarization analyzer is placed in front of the detector. Measuring the transmitted signal intensity while rotating the analyzer thus allows us to determine the polarization rotation.

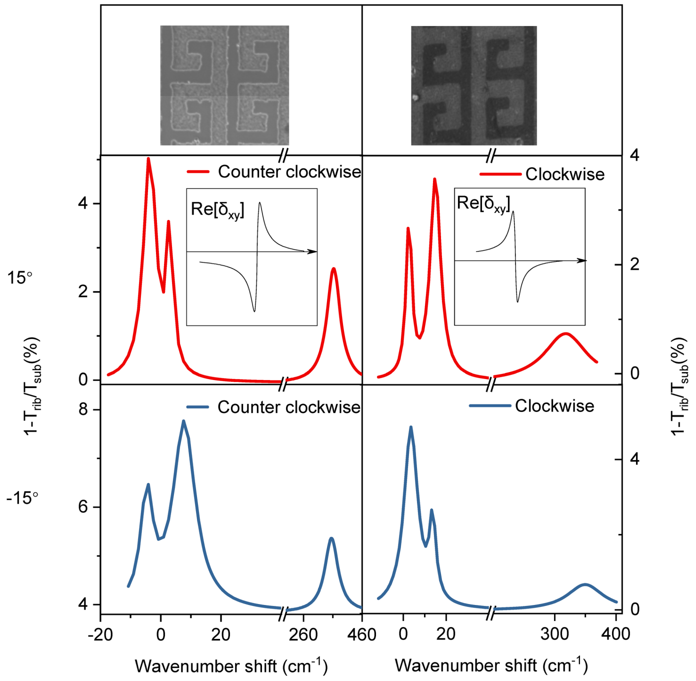

Extended Data Fig. 7 | Extinction spectra of CBP in counter clockwise and clockwise spiral ribbons. Opposite Faraday rotation angles are observed due to the Berry curvature is opposite for K and K′ valleys. Switching the sign of valley polarization by mirroring the spiral direction should reverse the sign of Faraday rotation.

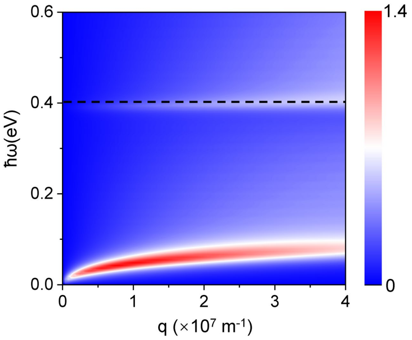

Extended Data Fig. 8 | Loss function calculation with Fermi energy at 0.05 eV ($n = 2 \times 10^{12}$ cm^{-2}). The dotted black line illustrates the quasi-flat dispersion of γ-mode.

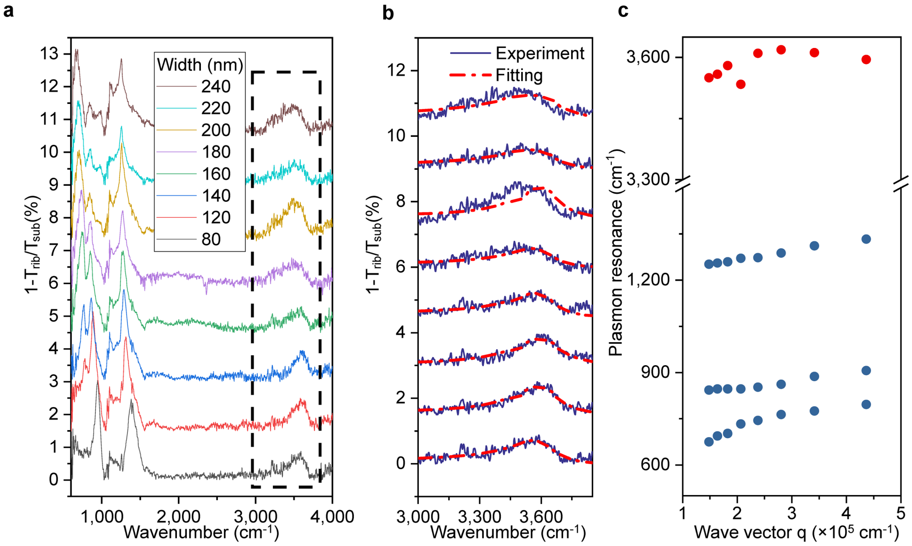

Extended Data Fig. 9 | Plasmon mode in 7.3° tBLG. **a**, Extinction spectra of tBLG ribbons on SiO$_2$ substrate with different ribbon widths. **b**, Enlarged extinction spectra of tBLG ribbons in the black dashed box. Blue curves are measured results. Red chain lines are best Fano fitting curves. **c**, Plasmon frequency as a function of wave vector for peaks in (a). The results show damped γ-mode.